Article

Mechanism of Surface-Enhanced Raman Scattering Based on 3D Graphene-TiO2 Nanocomposites and Application to Real-time Monitoring of Telomerase Activity in Differentiation of Stem Cells

Tingting Zheng, Enduo Feng, Zhiqiang Wang, Xue-Qing Gong, and Yang Tian

ACS Appl. Mater. Interfaces, **Just Accepted Manuscript** • DOI: 10.1021/acsami.7b11028 • Publication Date (Web): 05 Oct 2017

Mechanism of Surface-Enhanced Raman Scattering Based on 3D Graphene-TiO_2 Nanocomposites and Application to Real-time Monitoring of Telomerase Activity in Differentiation of Stem Cells

*Tingting Zheng,†,§ Enduo Feng, †,§ Zhiqiang Wang, ‡ Xueqing Gong, ‡ Yang Tian†,** †

†Department of Chemistry, School of Chemistry and Molecular Engineering, East China Normal University, Dongchuan Road 500, Shanghai 200241, China. E-mail: ytian@chem.ecnu.edu.cn

‡ Key Laboratory for Advanced Materials, Centre or computational Chemistry and Research Institute of Industrial Catalysis, School of Chemistry and Molecular Engineering, East China University of Science and Technology, 130 Meilong Road, Shanghai, 200237, P.R. China.

KEYWORDS: Surface-enhanced Raman scattering, graphene, TiO_2, telomerase activity, stem cells

ABSTRACT: With a burst development of new nanomaterials for plasmon-free surface-enhanced Raman scattering (SERS), the understanding of chemical mechanism and further applications have become more and more attractive. Herein, a novel SERS platform was specially designed through electrochemical deposition of graphene onto TiO_2 nanoarrays (EG-TiO_2). The developed EG-TiO_2 nanocomposites SERS platform possessed remarkable Raman activity using copper phthalocyanine (CuPc) as a probe molecule. XPS measurement revealed that the chemical bond Ti-O-C was formed at the interface between graphene and TiO_2 in EG-TiO_2 nanocomposites. Both experimental and theoretical results demonstrated that the obvious Raman enhancement was attributed to TiO_2-induced Fermi level shift of graphene, resulting in effective charge transfer between EG-TiO_2 nanocomposites and molecules. Taking advantage of marked Raman response of CuPc molecule on EG-TiO_2 nanocomposites surface as well as specific recognition of CuPc toward multiple telomeric G-quadruplex, EG-TiO_2 nanocomposites was tactfully employed as SERS substrate for selective and ultrasensitive determination of telomerase activity with low detection limit down to 2.07×10^{-16} IU. Interestingly, self-cleaning characteristic of EG-TiO_2 nanocomposites under visible light irradiation successfully provided a recycling ability for this plasmon-free EG-TiO_2 substrate. The present SERS biosensor with high analytical performance such as high selectivity and sensitivity, has been further explored to determine telomerase activity in stem cells, as well as to count the cell numbers. More importantly, using this useful tool, it was discovered that telomerase activity plays an important role in the proliferation and differentiation from human mesenchymal stem cells (hMSCs) to neural stem cells (NSCs). This work has not only established an approach for gaining fundamental insights into chemical mechanism (CM) of Raman enhancement, but also has opened a new way in investigation of long-term dynamic of stem cell differentiation and clinical drug screening.

INTRODUCTION

Surface-enhanced Raman scattering (SERS) is a widely studied and considered as a promising technique for microanalysis and trace species detection due to its remarkable advantages such as high sensitivity, nondestructive, quick response as well as providing unique information on the species. [1-3] Conventional SERS phenomenon is mainly attributed to electromagnetic field mechanism (EM) generated at the surface of noble metal such as Au and Ag, upon laser excitation. [4,5] Recently, another kind of Raman enhancement has been attracted more attention. The mechanism of this kind of Raman enhancement, named chemical mechanism (CM), is attributed to the chemical interaction between substrate and the adsorped molecules. The detailed mechanism of chemical Raman enhancement is actually poorly understood at the present stage. [6] The enhancement factors (EFs) originated for EM and CM depend on electromagnetic frequency resonance and molecule-substrate interaction, respectively. [7] EF values dominated by CM usually ranges from 10 to 100, [8,9] which is smaller than that obtained by the conventional SERS method. However, two dimensional SERS substrates originated from CM, including graphene, black phosphorus, hexagonal boron nitride, and molybdenum disulfide, have flat and smooth surfaces particularly suitable for selectively homogeneous deposition of aromatic molecules. Furthermore, the generated Raman signal is exclusive chemical enhancement, providing quantitative and specific analysis with high reproducibility and stability accessible. The star material among them is graphene, owing to its remarkable advantages, such as atomic uniformity, large delocalized bond, unique electronic structures, and chemical inertness. [10,11]

Herein, we developed a 3D material through electrochemical deposition of graphene onto TiO_2 nanoarrays (denoted as EG-TiO_2 nanocomposites), which show a remarkable enhancement of Raman scattering compared with native graphene or TiO_2 nanoarrays. Hybrid graphene and TiO_2

nanomaterials have received increasing attention due to their enhanced photoconversion efficiency, but it is the first time that EG-TiO_2 nanocomposites were developed for SERS substrate. From XPS data, it was found that Ti-O-C bond was formed on the interface between EG and TiO_2, confirming strong chemical interaction between electrodeposited graphene and TiO_2 nanoarrays. The theoretical and experimental results demonstrated that the electronic structures and Fermi levels of graphene clearly changed in EG-TiO_2 nanocomposites as compared with those of pure electrodeposited graphene (EG). Thus, remarkable Raman enhancement was observed at EG-TiO_2 nanocomposites due to highly efficient charge transfer from the shifted Fermi level to probe molecules. More interestingly, copper phthalocyanine (CuPc), which has a large Raman cross-section, was designed as the probe molecule. CuPc is a planar and π-conjugated molecule. [12] The exact electronic coupling of CuPc molecule to the "aromatic" EG-TiO_2 nanocomposites resulted in high molecular recognition ability. [13] Meanwhile, CuPc is a high affinity anionic ligand of G-quadruplex, [14] a four-stranded DNA structure with large planar aromatic rings (G-quartet) that forms from human telomere DNA consist of short tandem repeats of TTAGGG (in vertebrates). [15] On the other hand, telomere length homeostasis is maintained by telomerase, a ribonucleoprotein that synthesizes telomere repeats onto telomere ends to compensate the natural shortening of the telomeres. [16] The higher telomerase elongation efficiency leads to the greater number of G-quadruplexes. Therefore, intracellular telomerase activity can be tracked by Raman signal of CuPc attached to the G-quadruplexes. Specially, in this work, adopting our EG-TiO_2 SERS platform, the incorporation of CuPc into G-quadruplex telomere structures enabled SERS evaluation of telomerase activity with high sensitivity and selectivity. Significantly, for the first time, this unique SERS biosensor was successfully used in exploring the important role of telomerase activity plays in proliferation and differentiation capacity of stem cells.

RESULTS AND DISCUSSION

Development and Characterization of EG-TiO_2 Nanocomposites. The EG-TiO_2 nanocomposites were first designed and synthesized by electrodeposition of graphene onto TiO_2 nanoarrays. TiO_2 nanoarrays were fabricated using a facile two-step anodization process. [17] A top view scanning electron microscopic (SEM) image of TiO_2 nanoarrays in Figure 1a demonstrates high uniformity of the top nanoring structure in large scale. The magnified SEM image given in the inset of Figure 1a depicts clear periodical nanoring structure with an average diameter of ~200 nm and thickness of ~50 nm. The length of the nanotubes was controlled to ~1.5 μm (cross-section view of SEM image in Figure 1b), which may match the

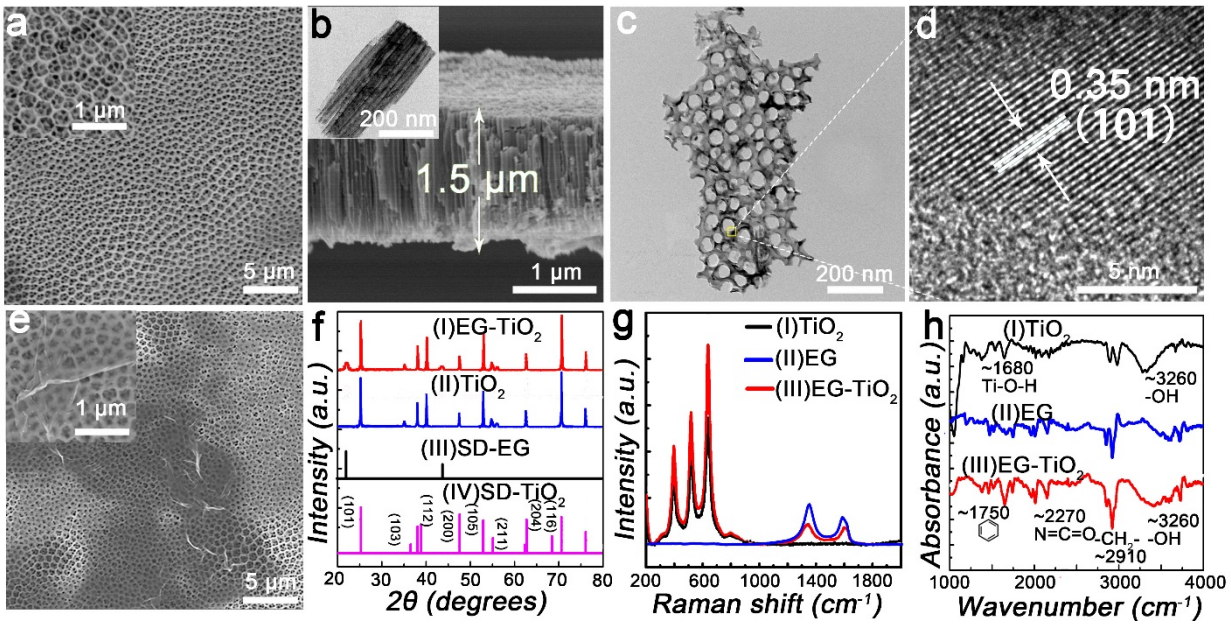

Figure 1. (a) Large-scale and magnification (inset) top view of SEM images of TiO_2 nanoarrays. (b) Cross-section SEM and TEM (inset) images of TiO_2 nanoarrays. (c) TEM image of top photonic nanorings of TiO_2 nanoarrays. (d) High resolution TEM image of TiO_2 nanoarrays. (e) Large-scale and magnification (inset) top view of SEM images of EG-TiO_2 platform. (f) XRD patterns (g) Raman spectra, and (h) FTIR spectra of (I) EG, (II) TiO_2 and (III) EG-TiO_2 nanoarrays.

maximum penetration depth of the incident light in TiO_2.[18] The top layer of TiO_2 nanoarrays with periodically nanoring structures was clearly observed in transmission electron microscopy (TEM) image of Figure 1c. High-resolution TEM (HRTEM) image (Figure 1d) demonstrates well-resolved lattice fringes with an inter-planar distance of 0.35 nm, which corresponds to (101) plane of anatase TiO_2. [19, 20] Then, graphene was electrochemically deposited onto the TiO_2 nanoarrays surface. [21] A typical cyclic voltammetry (CV) of graphene oxide (GO) electrolysis on TiO_2 nanoarrays was employed to track the electrodeposition process (Figure S1, Supporting Information). The cathodic peak I was attributed to the irreversible electro-chemical reduction of GO, while the cathodic peak II and the anodic peak III were ascribed to the redox pair of oxygen-containing groups on the graphene plane. [22] As shown in Figure 1e, a continuous and transparent graphene layer was well-coated on the surface of TiO_2 nanoarrays. Additionally, full-wavelength Raman spectrum of EG-TiO_2 nanocomposites (Figure S2a) was carried out to make a determination of the number of layers of graphene sheet. The Raman spectrum of EG-TiO_2 nanocomposites clearly showed a strong D band at 1330 cm^{-1}, a slightly weak G band at 1595 cm^{-1}relative to the D band and a very weak 2D band at 2710 cm^{-1}, which is the characteristic of single-layered oxidative graphene Raman spectra. [23] In other hand, AFM image of EG-TiO_2 (Figure S2b) with a thickness for ~0.6 nm also validated that graphene was deposited on TiO_2 as single layer. The crystalline structures of TiO_2 and EG-TiO_2 nanocomposites were further characterized by powder X-ray diffraction (XRD) spectroscopy (Figure 1f). A series of diffraction peaks were clearly observed at 25.28°, 37.80°, 38.58°, 48.05°, 53.89° and 55.06° in the wide-angle XRD pattern for TiO_2 nanoarrays, corresponding to (101), (004), (112), (200), (105) and (211) planes of anatase phase TiO_2 nanocrystals. [24] For EG-TiO_2 nanocomposites, two additional weak diffraction peaks were obtained at 21.2° and 43.3°, which were resulted from the electrodeposited

graphene as shown in Figure 1f. [25] Furthermore, as depicted in Figure 1g, both TiO_2 and EG-TiO_2 nanocomposites show characteristic Raman active modes at 397 cm^{-1}, 518 cm^{-1} and 640 cm^{-1}, corresponding to the existence of anatase phase. [26] However, two distinct peaks, D band at 1330 cm^{-1} and G band at 1595 cm^{-1}, both appeared at EG and EG-TiO_2 nanocomposites, indicating two typical Raman active vibration modes in graphitic structures. [10] In FTIR spectra (Figure 1h), compared to TiO_2 nanoarrays, EG-TiO_2 nanocomposites show additional infrared bands assigned to aromatic ring frame vibration at 1750 cm^{-1}, N=C=O stretching vibration at 2270 cm^{-1}, and the -CH_2- bending vibration at 2910 cm^{-1}. [27] Both Raman and FTIR results reveal that graphene has been successfully electrodeposited on the surface of TiO_2 nanoarrays.

More importantly, X-ray photoelectron spectroscopy (XPS) was performed to elucidate the chemical state of elements in EG-TiO_2 nanocomposites. From XPS survey spectrum shown in Figure. 2a, it is clear that EG-TiO_2 nanocomposites mainly consist of C, O and Ti without trace of contamination. The high-resolution XPS of C, O and Ti in EG, TiO_2 and EG-TiO_2 nanocomposites show distinct profiles (Figure 2b-d). The C 1s spectrum of EG is deconvoluted into C-C (non-oxygenated ring C, 284.6 eV), C-O (285.6 eV), and carbonyl O=C (carboxylic, 287.8 eV) species. [28] Binding energies of all these peaks, especially O=C energy, shift to higher energy levels in EG-TiO_2 nanocomposites (Figure 2b). On the other hand, the Ti core-level XPS spectrum in TiO_2 nanoarrays demonstrates two peaks centered at 458.5 and 464.2 eV (Figure 2c), which are assigned respectively to the Ti 2p1 and Ti 2p3 spin-orbital splitting photoelectrons in the Ti^{4+} state. [29] For EG-TiO_2 nanocomposites, these two peaks were observed at 459.3 and 465.0 eV, respectively. The splitting energy between two Ti-bands of these both samples was estimated to 5.7 eV, implying the presence of normal state of Ti^{4+}. [30] The difference of 0.8 eV between the Ti peak positions of TiO_2 and EG-TiO_2 nanocomposites was attributed to the interactions between

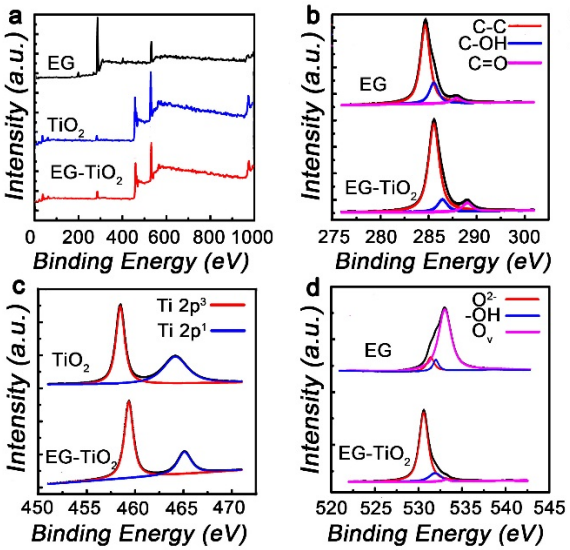

Figure 2. (a) XPS survey spectra of EG, TiO_2 and EG-TiO_2 nanocomposites. Core-level XPS spectra of (b) C1s, (c) Ti2p and (d) O1s of EG, TiO_2 and EG-TiO_2 nanocomposites.

Ti and oxygen centers of EG. Since oxygen, a highly electronegative element, withdrew the electron density from Ti of EG-TiO_2 nanocomposites. As a result, the binding energy of Ti in EG-TiO_2 nanocomposites increased compared with that in TiO_2.

To further support the presence of this binding, O1s core levels were also measured. As shown in Figure 2d, three peaks centered at 529.4, 530.0, 531.1 eV were clearly obtained, which were assigned to the presence of O^{2-}, -OH, and oxygen vacancies (O_v), respectively. [31] The greater ratios of O_v (68.15%) indicate more oxygen vacancies in EG, which are always coupling with Ti^{3+}. After binding with TiO_2, the peak of O_v decreased while O^{2-} increased, and binding energy of all these peaks shifted toward higher energy levels. In agreement with previous reports, this peak was assigned to binding energy of O in Ti-O-C bond. [32] Thus, it was confirmed that the Ti-O-C chemical bond was formed onto the interface between EG and TiO_2 in EG-TiO_2 nanocomposites.

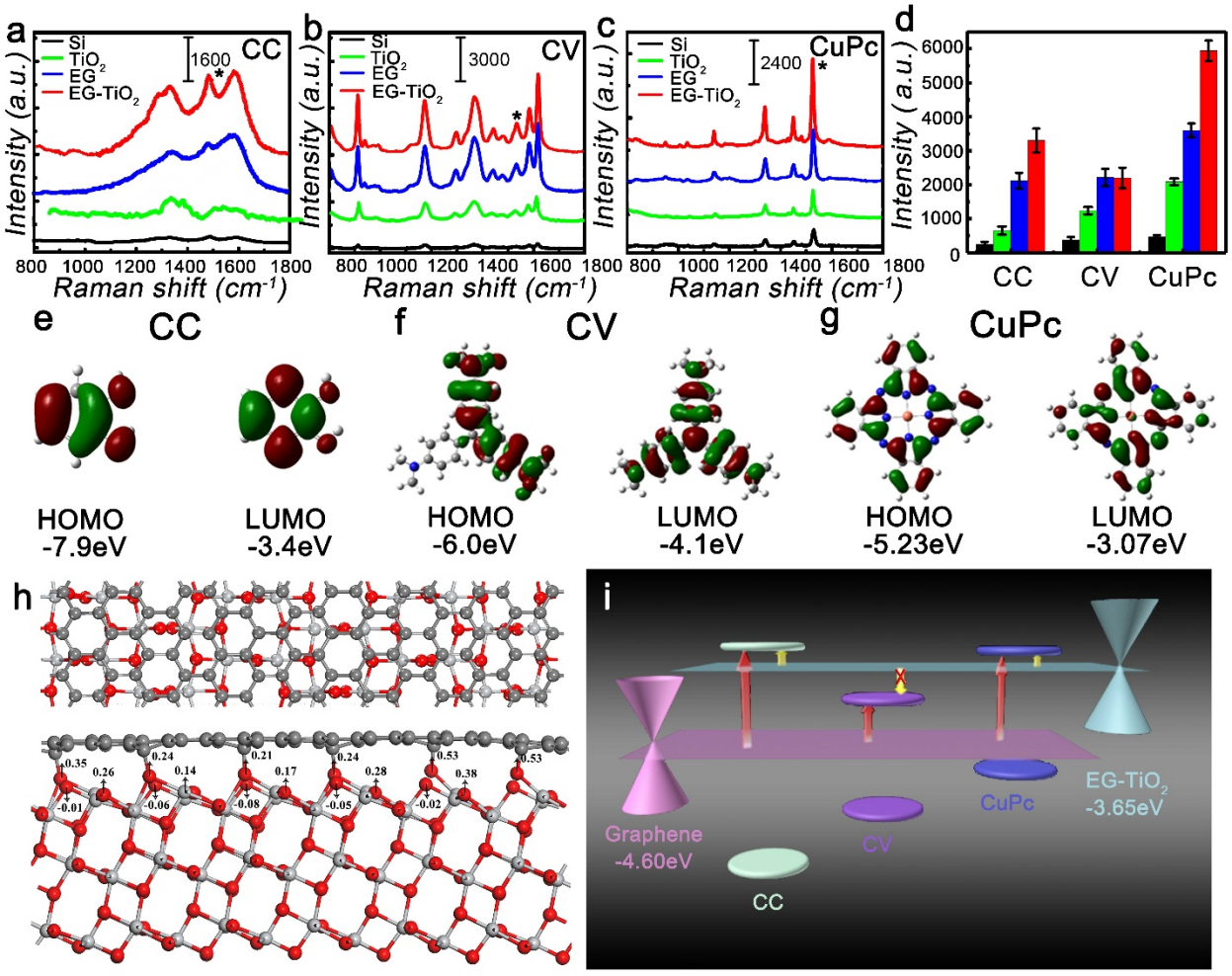

Figure 3. Raman spectra of (a) CC, (b) CV, and (c) CuPc on EG-TiO_2 nanocomposites (red line), EG (blue line), TiO_2 (green line) and on a blank SiO_2/Si substrate (black line) with the excitation laser wavelength of 633 nm. (d) Statistical data analysis for the comparison between the Raman intensity (1530 cm^{-1}) of CuPc CV and CC. Each data point represents the average value from three replicate SERS spectra (S.D., n= 6). Molecular structures and HOMO/LUMO energy levels of (e) CC, (f) CV, and (g) CuPc using DFT calculation. (h) Simulated models of EG-TiO_2 nanocomposites. Light grey, red, and dark grey, spheres represent Ti, O, and C atoms, respectively. The atoms in the surface layer of TiO_2 (001) have slight movement, and the positive (negative) values represent the atoms that slightly move upwards (push downwards). (i) Proposed mechanism for charge transfer of CC, CV and CuPc in EG and EG-TiO_2 platforms.

Mechanism of Raman Enhancement in EG-TiO_2 Nanocomposites. The effect of Raman enhancement with CM strongly depends on the matching degree of structure symmetry and energy level between molecules and substrates. [33] Figure 3a-c show Raman spectra of three typical symmetric molecules of D_{2h} (catechol, CC), C_3 (crystal violet, CV), and D_{4h} (copper phthalocyanine, CuPc) on EG-TiO_2 nanocomposites (red line), EG (blue line), TiO_2 (green line), and SiO_2/Si substrates (black line) under laser excitation of 633 nm. Obvious EFs were obtained on EG (9.7 for CC, 25.8 for CV and 20.5 for CuPc) and EG-TiO_2 nanocomposites (14.2 for CC, 24.6 for CV and 48.2 for CuPc) (Table S1) substrates, which were ascribed to symmetry matching between molecules of CC, CV, and CuPc with graphene substrate. On the contrary, no clear EFs were obtained for asymmetric molecules, such as oxalic acid, salicylic acid and dopamine (Figure S3, Supporting Information). Furthermore, the hexagonal lattice surface structure of EG-TiO_2 nanocomposites was similar to parallel-connected rings in the molecular structure of CV and CuPc. The structural similarity between both EG and EG-TiO_2 substrates and the molecules generally reduced the distance between molecules and substrates, thus strengthening the coupling. Such high symmetry and planar structure contribute to the obvious enhancement effects of CuPc and CV molecules on EG and EG-TiO_2 nanocomposites.

Focusing on 1530 cm^{-1} photon mode, the distortion vibration of the 16-membered macrocycle and benzene ring. [34] Figure 3d summarized the Raman intensity of CC, CV and CuPc at 1530cm^{-1}. It is very interesting that Raman scattering intensity was obviously enhanced on EG-TiO_2 nanocomposites for CuPc (~2.4 fold) and CC (~1.5 fold) molecules while that was slightly decreased for CV molecule, compared with those on EG substrate. Distinctly, the obvious changes should be ascribed to electronic structure between EG-TiO_2 nanocomposites and EG sheet. It is well-known that work function of graphene is larger than that of TiO_2. Thus, when EG is in contact

with an n-type semiconductor such as TiO_2, the charge distribution is readjusted for equilibration of Fermi level between EG and TiO_2, resulting in Fermi level elevation of EG to form a Schottky barrier (depletion layer) at the junction between these two materials. [35] Compared with the energy difference between Fermi level of EG nanocomposites and LUMO level of CuPc and CC, a smaller difference between Fermi level of EG-TiO_2 nanocomposites and LUMO level of CuPc and CC leads to more effective charge transfer between EG-TiO_2 nanocomposites and molecules, accordingly resulting in stronger Raman scattering.

To confirm the experimental results demonstrated above, the following model was employed, as shown in Figure 3g, for estimating Fermi level of EG-TiO_2 system: a 3×2 surface cell was used to construct a three-layer TiO_2 (101) slab, and a 3×7 surface cell for an EG slab. The valence atomic configure rations were Ti: $3d^2 4s^2$, O: $2s^2 2p^4$ and C: $2s^2 2p^2$, respectively. All calculations were performed using DFT methodologies implemented in the Vienna ab-initio simulation package (VASP). As demonstrated in Figure 3h, the Fermi level of EG-TiO_2 system was calculated to be situated at -3.65 eV, which is just between the calculated HOMO/LUMO levels of CuPc and CC. The energy difference between the Fermi level of EG-TiO_2 and LUMO levels of both molecules is smaller than that of EG resulting in an obvious Raman enhancement. Inversely, after introduction of TiO_2, the Fermi level of EG-TiO_2 nanocomposites shifted higher than LUMO level of CV, leading to a slight decline of Raman intensity.

Furthermore, the match between excitation laser energy and HOMO/LUMO gap of molecules is also an important factor for Raman enhancement. HOMO/LUMO gaps of CV and CuPc were estimated to be 1.9 eV and 1.7 eV, respectively, using density functional theory (DFT) (Figure 3d-e). For CuPc and CV under 633 nm (1.96 eV) laser excitation, the EFs are stronger than under 532 nm (2.33 eV) laser excitation (Table S2), possibly because the 532 nm laser excitation is not in the

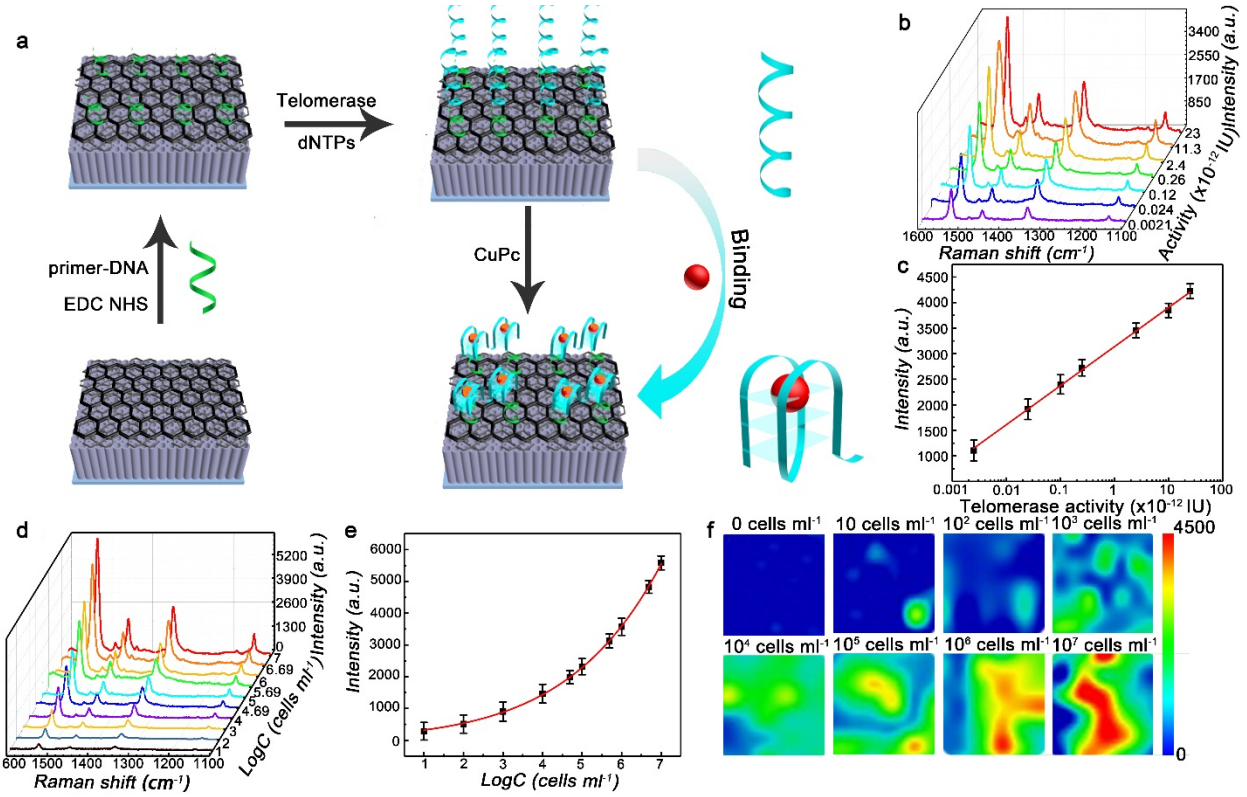

Figure 4. (a) Schematic illustration for working principle of the developed SERS platform based on EG-TiO_2 nanocomposites for determination of telomerase activity. (b) Raman spectra of the developed EG-TiO_2 nanocomposites SERS biosensor obtained with telomerase activity of 1.0, 1.5, 2.0, 2.5, 3.0, 3.5, 4.0, 4.5, 5.0 IU L^{-1}(c) Plot of Raman scattering intensity *vs* telomerase activity. Each data point represents the average value from three replicate SERS spectra (S.D., n= 6). (d) Raman spectra of the EG-TiO_2 nanocomposites SERS biosensor obtained with hMSC concentrations of 10, 10^2, 10^3, 10^4, 10^5, 10^6, 10^7 cells mL^{-1}. (e) Plot of Raman scattering intensity vs logarithm of hMSC concentration. Each data point represents the average value from three replicate SERS spectra (S.D., n= 6). Error bars equal to the standard deviations. (f) SERS imaging of telomerase activity obtained with different hMSC concentrations.

resonance window with the HOMO/LUMO energy gap of CuPc and CV. [25] On the contrary, CC has a HOMO/LUMO gap of 4.4 eV (Figure 3f), which is too large to be resonant with 532 or 633

nm laser excitation. Consequently, no obvious SERS effects were observed for CC under 532 or 633 nm excitation.

Imaging and Biosensing of Telomerase Activity in Human Mesenchymal Stem Cells (hMSCs). Besides the high molecular recognition ability of EG-TiO_2 nanocomposites SERS substrate toward CuPc demonstrated above, CuPc is a high affinity anionic ligand of G-quadruplex, which can be produced from human telomere repeats (TTAGGG)n. Therefore, the developed EG-TiO_2 nanocomposites was employed as enhanced Raman substrate for both selective and quantitative characterization of telomerase activity as well as for counting of cell numbers using CuPc as a specific recognition element. Figure 4a illustrates the major steps involved in the working principle of the present SERS biosensor for determination of telomerase activity based on EG-TiO_2 nanocomposites substrate. Amino-modified telomerase primers were first immobilized on EG-TiO_2 nanocomposites and extended by telomerase to form telomere repeats (TTAGGG)n. The extension of primer caused by telomerase was verified by gel electrophoresis (Figure S4, Supporting Information). Then, the guanine (G)-rich sequences undergo conformational changes to form a G-quadruplex, [36] which exhibits high selectivity and affinity for CuPc (K_d = 42 M in the presence of 100 mM KCl). [37] In this way, intracellular telomerase activity can be tracked through Raman signal of CuPc. The stepwise assembly process of the developed SERS biosensor was monitored by electrochemical impedance spectroscopy (EIS) measurements (Figure S5, Supporting Information), which indicated a successful fabrication of SERS biosensor.

After optimizing the experimental conditions (Figure S6, Supporting Information), the activity of pure telomerase was subsequently evaluated by the proposed approach to validate sensitivity and selectivity of this strategy. To exclude unexpected backgrounds which were caused by non-specific adsorption of CuPc, we firstly synthesized a DNA sequence 5'-NH_2- AAT CCG TCG AGC AGA

GTT TTA GGG TTA GGG TTA GGG-3', to simulate the elongated primer sequence by telomerase. As shown in Figure S7a, a very weak Raman signal was obtained from the platform with primer, while a significant enhancement was observed with E-primer. Furthermore, we also employed UV-Vis spectra to explore the non-specific adsorptions of CuPc. CuPc molecules could absorb incident UV-Vis light and showed two obvious adsorption peaks at 620 nm and 690 nm, respectively. Figure S7b showed the representative spectra of EG-TiO_2. An obvious adsorption peak both at ~620 nm and 690 nm were observed for the E-primer modified EG-TiO_2. On the contrary, no obvious adsorption peak in the range of 600 nm-700 nm for the primer modified EG-TiO_2. Together with the comparison of Raman spectra, these results indicated that there were few non-specific adsorptions of CuPc on the EG-TiO_2 nanocomposites. In addition, because of the presence of G-quadruplex between CuPc molecules and EG-TiO_2 nanocomposites, the enhancement effect of EG-TiO_2 nanocomposites for CuPc might be affect. To confirm the influence of the DNA nanostructures to Raman signal, we conducted an additional experimental comparison with/without the presence of DNA nanostructures in Figure S7a. There were not obvious differences under these two different conditions, which reflected that DNA nanostructures had negligible influences to the Raman signals.

As shown in Figure 4b, Raman scattering intensity increased with the increasing concentration of telomerase. The characteristic peak around 1529 cm^{-1} was employed to directly probe CuPc attached onto EG-TiO_2 nanocomposites, and thus to determine telomerase activity. The calibration curve displays a linear relationship between Raman scattering intensity (I) and telomerase activity (A) over the range of $2.1x10^{-15}$ IU to $2.3x10^{-11}$ IU in a single cell (R =0.998, n = 7) (Figure 4c). The linear regression equation was

$$I = 3.905\times10^{3} + 763.6 \lg (A\times10^{12}) \text{ (IU)} \qquad (1)$$

The detection limit was achieved down to be 2.07×10^{-16} IU at 3σ, which is much lower than other approach for detection of telomerase .[38,39]

A critical length of telomere repeats is required to ensure proper telomere function and avoid the activation of DNA damage pathways that results in replicative senescence or cell death. As hMSCs have elongated proliferative capacity, telomerase activity level is important to maintain telomere length through many cell divisions. Herein, the proposed EG-TiO_2 nanocomposites platform was further used for hMSC counting as well as evaluation the role telomerase activity played in the proliferation process of hMSCs. Figure 4d displays the Raman signal of biosensor corresponding to the 1st generation hMSCs at different concentrations. The Raman intensity increased monotonically with the logarithm concentration of hMSCs as shown in Figure 4e, and the detection limit was determined to be ~10 cells mL^{-1} at 3σ. As 100 μL of cell suspension was used for incubation, our approach was used to realize the telomerase activity measurement down to 1 hMSC, which was significantly lower than those electrochemical and fluorescent cytosensing approaches. [40] A topographic image of 100×100 μm^2 was also collected from the integrated intensity of 1529 cm^{-1} peak. As demonstrated in Figure 4f, Raman signals of the developed SERS biosensor for telomerase activity remarkably increased with the increasing concentration of cells. However, negligible Raman signal changes were observed for this SERS biosensor incubated with PBS. The results suggest that CuPc can successfully attach to G-quadruplex extended by telomerase from cell extracts with high selectivity.

Recyclability of EG-TiO_2 Nanocomposites SERS **Biosensor.** As well-known, TiO_2 shows UV-vis absorption in the range of 200-350 nm, [41] which was also confirmed in Figure S8 (Supporting Information). However, absorbance of EG-TiO_2 nanocomposites obviously decreased in UV region while increased in visible region (400-700 nm) (Figure S9, Supporting Information), which

was attributed to the shift of Fermi level in EG-TiO_2 nanocomposites, Thus, the recyclability test of this SERS biosensor was carried out by irradiation using a Xe light source (Asahi Spectra, LAX-C100) through the filters (460 nm $<\lambda<$ 700 nm, 1000W/m^2) onto EG-TiO_2 nanocomposites. [42] Figure S9a (Supporting Information) shows Raman spectra before and after illuminated by visible light on EG-TiO_2 nanocomposites substrate. It was found that all Raman peaks of CuPc disappeared after irradiation for 90 min, indicating that CuPc was completely photodegraded. By contrast, negligible changes were observed for Raman intensity of CuPc on bare TiO_2 nanoarrays after irradiation for 90 min (Figure S9b, c Supporting Information). The rapid and efficient self-cleaning ability should be attributed to change of energy band of EG-TiO_2 nanocomposites structure after electrochemical deposition of graphene onto TiO_2 nanoarrays. After 5 cycles of modification followed by irradiation, the SERS activity of EG-TiO_2 substrate was still able to reach more than 98%, compared with the original one, revealing the excellent reproducibility and recyclability of EG-TiO_2 substrate in SERS monitoring (Figure S9d, Supporting Information).

Important Role of Telomerase Activity in Proliferation and Differentiation of Stem Cells. The sensitive and recyclable EG-TiO_2 nanocomposites SERS biosensor demonstrated above were further used to explore the role of telomerase activity plays in proliferation and differentiation capacity of hMSCs into neural stem cells (NSCs). NSC provides an alternative and attractive cell source for neuroregeneration, the leading trophic factor candidate so far identified for treatment of Parkinson disease (PD). [43] One of the NSC sources is differentiation from hMSCs, which are easy-based, more primitive and not limited by ethical and legal. [44] Telomerase activity plays an important role in this cell differentiation and activation. [45] However, how telomerase activity affects the differentiation process from hMSCs to NSCs has never been reported yet. In this work,

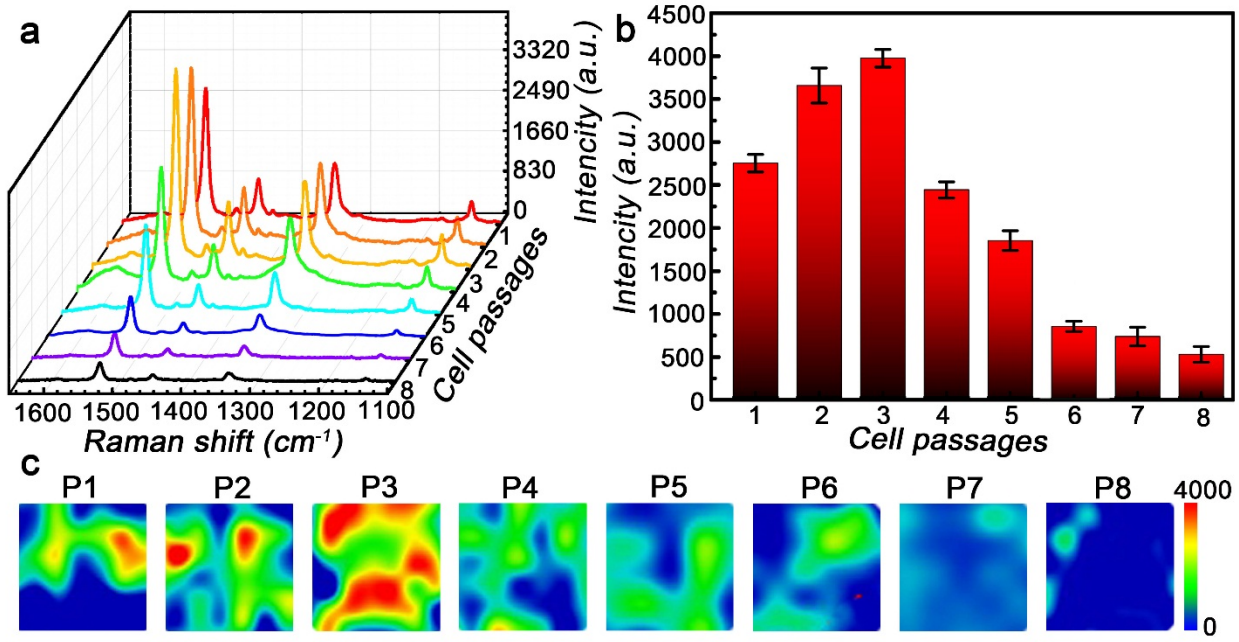

Figure 5. (a) Raman spectra of the developed EG-TiO_2 nanocomposites SERS biosensor in response to telomerase activity from different generations of hMSCs. (b) Raman scattering intensity (~1529 cm^{-1}) versus different generations of hMSCs. The error bars represent the standard deviation obtained from measurements performed on the SERS sensor. (c) SERS imaging of telomerase activity of different generations of hMSCs.

telomerase activity of different generations of hMSCs was evaluated in detail to demonstrate the important role of telomerase plays in the differentiation process from hMSCs into NSCs. With the proliferation of hMSCs, Raman scattering intensity gradually increased and reached the maximum at the 3rd generation, (the telomerase activity in a single hMSC was calculated to be 2.4×10^{-12} IU)

(Figure 5). Afterwards, Raman signal gradually decreased and almost faded away until the 6th generation. In this case, telomerase activity shows a positive expression in the first five generations of hMSC, and reached a maximum in the 3rd generation, which was consistent with the results of commercial ELISA kit (Figure S10, Supporting Information). To demonstrate the crucial role of

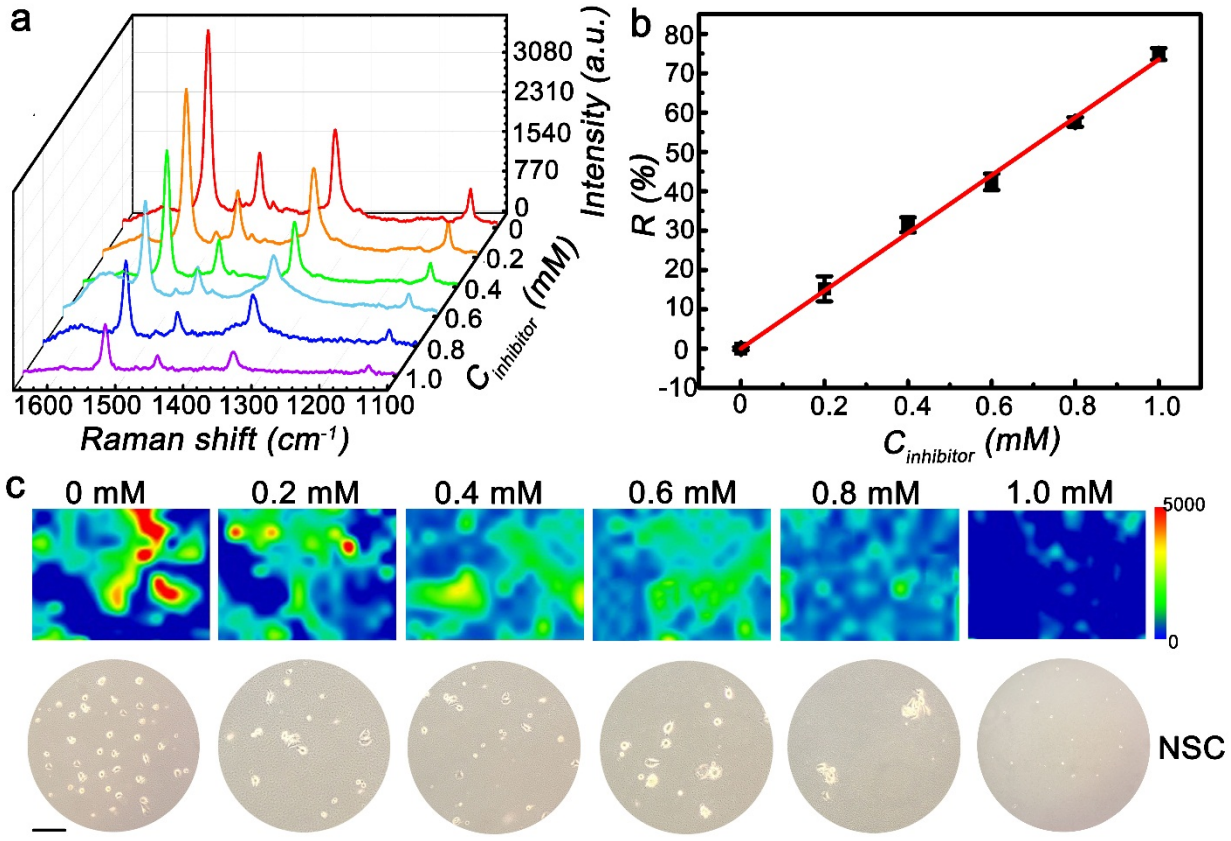

Figure 6. (a) Raman spectra of the EG-TiO_2 nanocomposites SERS biosensor in response to telomerase activity from the 3rd of hMSCs treated with inhibitor AZT with various concentrations for 24 h. (b) Relationship between the decreased Raman scattering intensity (*I*) and concentration of inhibitor AZT. Error bars represent one standard deviation for three independent measurements (S.D., n=3). (c) SERS imaging of telomerase activity in response to telomerase extracts from hMSC (P3) which were treated with inhibitor of various concentration and the bright-field images of NSC which were induced from hMSC (P3) treated with inhibitor of various concentration. All bright-field images in panel C share the same scale bar (50μm)

telomerase activity in the differentiation process, hMSCs were induced by human basic fibroblast growth factor and human epidermal growth factor (Figure S11, Supporting Information). As shown in Figure S12 (Supporting Information), hMSCs were able to differentiate into NSCs till

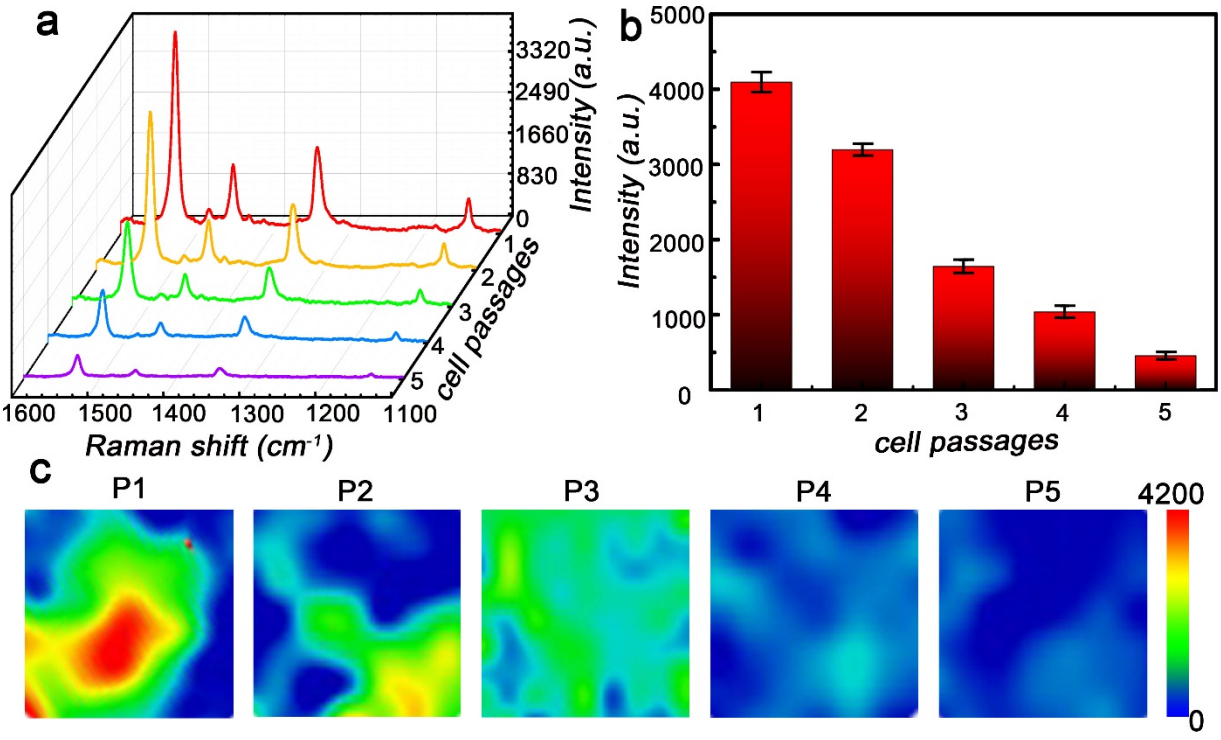

Figure 7. (A) Raman spectra of EG-TiO_2 nanocomposites SERS in response to telomerase activity from different passages of NSCs differentiated from the 3rd generation of hMSCs. (B) Raman scattering intensity (1529 cm^{-1}) versus different generations of NSCs differentiated from the 3rd generation of hMSCs. (C) SERS imaging of telomerase activity of different generations of NSCs differentiated from the 3rd generation of hMSCs.

the 5th generation and the 3rd generation of hMSCs differentiated the best state of NSCs, which were in a good agreement with the above results. To further assess the specificity of this strategy, a common telomerase inhibitor 3'-azido-3'-.deoxythymidine (AZT) was employed. As expected, Raman scattering intensity with regard to telomerase activity in the presence of AZT was much lower than that in the absence of AZT (Figure 6a). Moreover, Raman scattering intensity decreased towards increasing concentration of inhibitor, revealing that the change of Raman scattering intensity was indeed ascribed to telomerase activity. The concentration-dependent inhibition of telomerase activity by AZT was presented in Figure 6b in terms of decreasing percentage of Raman

scattering intensity (R). R was calculated by $100(I_0-I_n)/I_0$, where, I_n and I_0 stand for Raman scattering intensity measured for cells treated with and without AZT, respectively. The value of R increased proportionally with increasing concentration of AZT, indicating a stepwise inhibition of telomerase and the detection limit was achieved to 0.06 mM.

Telomerase activity of different generations of NSCs differentiated from the first five passages of hMSC were also monitored using this EG-TiO_2 nanocomposites SERS platform. As shown in Figure 7 and Figure S13 (Supporting Information), a positive telomerase expression was observed in the first four generations of differentiated NSCs, which was consistent with the result of commercial ELISA kit (Figure S14, Supporting Information). However, superior to the commercial ELISA kit, our EG-TiO_2 nanocomposites SERS biosensor offered the advantages of high sensitivity, simplicity, rapid response, and low cost. In addition, telomerase activity decreased with increasing generation of NSCs, which results in that NSCs cannot be passaged for a long time.48 It was also found that the effect of the 1st generation of NSCs transplantation on spinal cord injury was better than that of other NSCs. Consequently, all these results demonstrate that telomerase activity plays an important part during the proliferation and differentiation processes for NSCs.

CONCLUSION

In this work, we have first successfully developed a plasmon-free EG-TiO_2 nanocomposites SERS platform for in-situ monitoring of telomerase activity in the proliferation and differentiation processes from hMSCs to NSCs. XPS data have demonstrated that Ti-O-C chemical bond was formed at the interface between EG and TiO_2 nanoarrays, confirming strong chemical interaction between graphene and TiO_2 in EG-TiO_2 nanocomposites, rather than physical adsorption and

electrostatic interaction. The experimental and theoretical results have revealed that remarkable Raman enhancement at EG-TiO_2 nanocomposites are attributed to TiO_2-induced Fermi level elevation of graphene, and consequently resulting in the change of the energy band degree between EG-TiO_2 nanocomposites substrate and molecules. More interestingly, by designing CuPc as a specific recognition element toward telomerase activity, the EG-TiO_2 nanocomposites SERS platform has been successfully explored for sensitive and quantitative determination of telomerase activity during the expansion and differentiation processes of hMSCs for the first time. The detection limit is achieved down to 2.07×10^{-16} IU with quick response within 2 min. In addition, the self-cleaning characteristic of EG-TiO_2 nanocomposites under visible light illumination, which is originated from the change of energy band of EG-TiO_2 composites has realized the recycling of EG-TiO_2 nanocomposites SERS substrate. The remarkable analytical performance, together with good biocompatibility, and long-term stability and recycling ability, has opened up a new approach to evaluate the important role of telomerase activity plays in proliferation and differentiation processes from hMSCs to NSCs. The present investigation has not only provided a methodology for development of 3D hybrid nanomaterials for enhanced Raman scattering, but also established a model for deep understanding chemical mechanism in SERS. Moreover, this 3D-based SERS substrate can be easily extended to broad applications in clinical diagnosis and biomedical treatments for stem cell with great potentials.

ASSOCIATED CONTENT

Supporting Information

Experimental details, SERS spectra of asymmetric molecules, assembly process and recyclability of EG-TiO_2 nanocomposites SERS biosensor, ELISA kit detection of telomerase, the

differentiation process of hMSCs, EF values of different molecules on various SERS substrates were characterized. This material is available free of charge via the Internet at http://pubs.acs.org.

AUTHOR INFORMATION

Corresponding Author

* ytian@chem.ecnu.edu.cn

Present Addresses

† Department of Chemistry, School of Chemistry and Molecular Engineering, East China Normal University, Dongchuan Road 500, Shanghai 200241, China.

‡ Key Laboratory for Advanced Materials, Centre or computational Chemistry and Research Institute of Industrial Catalysis, School of Chemistry and Molecular Engineering, East China University of Science and Technology, 130 Meilong Road, Shanghai, 200237, P.R. China.

Author Contributions

§ T. Z. and E. F. equally contributed to this work.

Notes

The authors declare no competing financial interest.

ACKNOWLEDGMENT

The authors greatly appreciate the financial support from National Natural Science Foundation of China for distinguished Young Scholars (21325521) and NNSFC (21635003, 21175098 and 21605049). The Program of Shanghai Subject Chief Scientist (15XD1501600) and Shanghai Sailing Program (16YF1402700) are gratefully acknowledged.

REFERENCES

1. Lee, H.; Lee, J. H.; Jin, S. M.; Suh, Y. D.; Nam, J. M. Single-Molecule and Single-Particle-Based Correlation Studies between Localized Surface Plasmons of Dimeric Nanostructures with ~1 nm Gap and Surface-Enhanced Raman Scattering. *Nano Lett.* **2013**, *13*, 6113-6121.

2. Xu, L. J.; Lei, Z. C.; Li, J. X.; Zong, C.; Yang, C. Y. J.; Ren, B. Label-Free Surface-Enhanced Raman Spectroscopy Detection of DNA With Single-Base Sensitivity. *J. Am. Chem. Soc.* **2015**, *137*, 5149−5154.

3. Ding, S. Y.; Yi, J.; Li, J. F.; Ren, B.; Wu, D. Y.; Panneerselvam, R.; Tian, Z. Q. Nanostructure-Based Plasmon-Enhanced Raman Spectroscopy for Surface Analysis of Materials. *Nat. Rev. Mater*. **2016**, *1*, 16021

4. Mo, A. H.; Landon, P. B.; Gomez, K. S.; Kang, H.; Lee, J.; Zhang, C.; Janetanakit, W.; Sant, V.; Lu, T.; Colburn, D. A.; Akkiraju, S.; Dossou, S.; Cao, Y.; Lee, K. F.; Varghese, S.; Glinskyc. G.; Lal. R. Magnetically-Responsive Silica–Gold Nanobowls for Targeted Delivery and SERS-Based Sensing. *Nanoscale* **2016**, *8*, 11840-11850.

5. Abdelsalam, M. E.; Mahajan, S.; Bartlett, N. P.; Baumberg, J. J.; Russell, A. E. SERS at Structured Palladium and Platinum Surfaces. *J. Am. Chem. Soc.* **2007**, *129*, 7399-7406

6. Alessandri, I.; Biavardi, E.; Gianoncelli, A.; Bergese, P.; Dalcanale, E. Cavitands Endow All-Dielectric Beads with Selectivity for Plasmon-Free Enhanced Raman Detection of N ε-Methylated Lysine. *ACS Appl. Mater. Interfaces* **2016**, *8*, 14944−14951.

7. Bakker, R. M.; Permyakov, D.; Yu, Y. F.; Markovich, D.; Paniagua-Dominguez, R.; Gonzaga, L.; Samusev, A.; Kivshar, Y.; Luk'yanchuk, B.; Kuznetsov, A. I. Magnetic and Electric Hotspots with Silicon Nanodimers. *Nano Lett.* **2015**, *15*, 2137−2142.

8. Huang, C. S.; Kim, M. W.; Wong, B. M.; Safron, N. S.; Arnold, M. S.; Gopalan, P. Raman Enhancement of a Dipolar Molecule on Graphene. *J. Phys. Chem. C* **2014**, *118*, 2077−2084.

9. Carboni, D.; Lasio, B.; Alzari, V.; Mariani, A.; Loche, D.; Casula, M. F.; Malfatti, L.; Innocenzi, P. Graphene-Mediated Surface Enhanced Raman Scattering in Silica Mesoporous Nanocomposite Films. *Phys. Chem. Chem. Phys.* **2014**, *16*, 25809-25818.

10. Xu, W. G.; Mao, N. N.; Zhang, J. Graphene: A Platform for Surface‐Enhanced Raman Spectroscopy. *Small* **2013**, *9*, 1206-1224.

11. Xu, W.; Ling, X.; Xiao, J.; Dresselhaus, M. S.; Kong, J.; Xu, H.; Liu, Z.; Zhang, J. Surface Enhanced Raman Spectroscopy on A Flat Graphene Surface. *Proc. Natl. Acad. Sci. U. S. A.* **2012**, *109*, 9281–9286.

12. Uemura, T.; Furumoto, M.; Nakano, T.; Akai-Kasaya, M.; Salto, A.; Aono, M.; Kuwahara, Y. Local-Plasmon-Enhanced Up-Conversion Fluorescence from Copper Phthalocyanine. *Chem. Phys. Lett.* **2007**, *448*, 232–236.

13. Huang, S. X.; Ling, X.; Liang, L. B.; Song, Y.; Fang, W. J.; Zhang, J.; Kong, J.; Meunier, V.; Dresselhaus, M. S. Molecular Selectivity of Graphene-Enhanced Raman Scattering. *Nano Lett.* **2015**, *15*, 2892−2901.

14. Yaku, H.; Murashima, T.; Miyoshi, D.; Sugimoto, N. Anionic Phthalocyanines Targeting G-Quadruplexes and Inhibiting Telomerase Activity in The Presence of Excessive DNA Duplexes. *Chem. Commun.* **2010**, *46*, 5740–5742.

15. Liu, Y.; Wei, J. M.; Liu, X.; Wei, W.; Zhao, H. Y.; Zhang, Y. J.; Liu, S. Q. Label-Free Ultrasensitive Detection of Telomerase Activity Via Multiple Telomeric Hemin/G-Quadruplex Triggered Polyaniline Deposition and A DNA Tetrahedron-Structure Regulated Signal. *Chem. Commun.* **2016**, *52*, 1796.

16. Blackburn, E. H. Structure and Function of Telomeres. *Nature* **1991**, *350*, 569−573.

17. Zhang, Z.; Wang, H. P. Optimization of Photoelectrochemical Water Splitting Performance on Hierarchical TiO_2 Nanotube Arrays. *Energy Environ. Sci.* **2012**, *5*, 6506−6512.

18. Lynch, R. P.; Ghicov, A.; Schmuki, P. A. A Photo-Electrochemical Investigation of Self-Organized TiO_2 Nanotubes. *J. Electrochem. Soc.* **2010**, *157*, G76−G84.

19. Liao, J. Y.; Lei, B. X.; Chen, H. Y.; Kuang, D. B.; Su, C. Y. Oriented Hierarchical Single Crystalline Anatase TiO_2 Nanowire Arrays on Ti-Foil Substrate for Efficient Flexible Dye-Sensitized Solar Cells. *Energy Environ. Sci.* **2012**, *5*, 5750−5757.

20. Sordello, F.; Odorici, E.; Hu, K.; Minero, C.; Cerruti, M.; Calza, P. Shape Controllers Enhance the Efficiency of Graphene-TiO_2 Hybrids in Pollutant Abatement. *Nanoscale* **2016**, *8*, 3407-3415.

21. Zhang, Y.; Zeng, G. M.; Tang, L.; Chen, J.; Zhu, Y. He, X. X.; He, Y. Electrochemical Sensor Based on Electrodeposited Graphene-Au Modified Electrode and Nano Au Carrier Amplified Signal Strategy for Attomolar Mercury Detection. *Anal. Chem.* **2015**, *87*, 989–996

22. Chen, L. Y.; Tang, Y. H.; Wang, K.; Liu, C. B.; Luo, S. L. Direct Electrodeposition of Reduced Graphene Oxide on Glassy Carbon Electrode and Its Electrochemical Application. *Electrochem. Commun.* **2011**, *13*, 133–137.

23. Kim, S.; Ku, S. H.; Lim, S. Y.; Kim, J. H.; Park, C. B. Graphene–Biomineral Hybrid Materials. *Adv. Mater.* **2011**, *23*, 2009–2014.

24. Ding, J.; Huang, Z. N.; Zhu, J. H.; Kou, S. Z.; Zhang, X. B.; Yang, H. S. Low-Temperature Synthesis of High-Ordered Anatase TiO_2 Nanotube Array Films Coated with Exposed {001} Nanofacets. *Sci. Rep*. **2015**, *5*, 17773.

25. Yan, Y.; Yin, Y. X.; Guo, Y. G.; Wan, L. J. A Sandwich-Like Hierarchically Porous Carbon/Graphene Composite as a High-Performance Anode Material for Sodium-Ion Batteries. *Adv. Energy Mater.* **2014**, *4*, 1301584.

26. Mo, R.; Lei, Z.; Sun, K.; Rooney, D. Facile Synthesis of Anatase TiO_2 Quantum-Dot/Graphene-Nanosheet Composites with Enhanced Electrochemical Performance for Lithium-Ion Batteries. *Adv. Mater.* **2014**, *26*, 2084-2088.

27. Ji, Z. Q.; Wu, R.; Adamska, L. L.; Velizhanin, K. A.; Doorn, S. K.; Sykora, M. In Situ Synthesis of Graphene Molecules on TiO_2: Application in Sensitized Solar Cells. *ACS Appl. Mater. Interfaces* **2014**, *6*, 20473−20478.

28. Cao, S. Y.; Liu, T. G.; Tsang, Y. H.; Chen, C. S. Role of Hydroxylation Modification on The Structure and Property of Reduced Graphene Oxide/TiO_2 Hybrids. *Appl. Surf. Sci.* **2016**, *382*, 225-238.

29. Sher Shah, M. S. A.; Park, A. R.; Zhang, K.; Park, J. H.; Yoo, P. J. Green Synthesis of Biphasic TiO_2–Reduced Graphene Oxide Nanocomposites with Highly Enhanced Photocatalytic Activity. *ACS Appl. Mater. Interfaces* **2012**, *4*, 3893−3901.

30. Bajestani, Z. G.; Yürüm, A.; Yürüm, Y. Significant Improvement in The Hydrogen Storage Capacity of a Reduced Graphene Oxide/Tio_2 Nanocomposite by Chemical Bonding of Ti–O–C. *RSC Adv*. **2016**, *6*, 32831–32838.

31. Qi, D. Y.; Lu, L. J.; Xi, Z. H.; Wang, L. Z.; Zhang, J. L. Enhanced Photocatalytic Performance of TiO_2 Based on Synergistic Effect of Ti^{3+} Self-Doping and Slow Light Effect. *Appl. Catal., B* **2014***, 160−161,* 621−628.

32. Wang, W. S.; Wang, D. H.; Qu, W. G.; Lu, L. Q.; Xu, A. W. Large Ultrathin Anatase TiO_2 Nanosheets With Exposed {001} Facets on Graphene for Enhanced Visible Light Photocatalytic Activity. *J. Phys. Chem. C* **2012**, *116*, 19893–19901.

33. Ling, X.; Xie, L. M.; Fang, Y.; Xu, H.; Zhang, H. L.; Kong, J.; Dresselhaus, M. S.; Zhang, J.; Liu, Z. F. Can Graphene Be Used as A Substrate for Raman Enhancement? *Nano Lett.* **2010**, *10*, 553-561.

34. Cerdeira, F.; Garriga, M.; Alonso, M. I.; Ossó, J. O.; Schreiber, F.; Dosch, H.; Cardona, M. Raman Spectroscopy as A Probe Of Molecular Order, Orientation, and Stacking Of Fluorinated Copper-Phthalocyanine (F_{16}cupc) Thin Films. *J. Raman Spectrosc.* **2013**, *44*, 597−607.

35. Jiang, X.; Li, X. L.; Jia, X. F.; Li, G. Z.; Wang, X.; Wang, G. Y.; Li, Z. S.; Yang, L. B.; Zhao, B. Surface-Enhanced Raman Scattering from Synergistic Contribution of Metal and

Semiconductor in TiO_2/MBA/Ag (Au) and Ag (Au)/MBA/TiO_2 Assemblies. *J. Phys. Chem. C* **2012**, *116*, 14650−14655.

36. Neidle, S. Human Telomeric G-Quadruplex: The Current Status of Telomeric G-Quadruplexes as Therapeutic Targets In Human Cancer. *FEBS J*. **2010**, *277*, 1118-1125.

37. Yaku, H.; Murashima, T.; Miyoshi, D.; Sugimoto, N. Specific Binding of Anionic Porphyrin and Phthalocyanine To The G-Quadruplex with A Variety Of In Vitro And In Vivo Applications. *Molecules* **2012**, *17*, 10586-10613.

38. Xu, L. G.; Zhao, S.; Ma, W.; Wu, X. L.; Li, S.; Kuang, H.; Wang, L. B.; Xu, C. L. Multigaps Embedded Nanoassemblies Enhance in Situ Raman Spectroscopy for Intracellular Telomerase Activity Sensing. *Adv. Funct. Mater.* **2016**, *26*, 1602–1608

39. Zong, S. F.; Wang, Z. Y.; Chen, H.; Hu, G. H.; Liu, M.; Chen, P.; Cui, Y. P. Colorimetry and SERS Dual-Mode Detection of Telomerase Activity: Combining Rapid Screening with High Sensitivity. *Nanoscale*, **2014**, *6*, 1808

40. Liu, X.; Wei, M.; Xu, E. S.; Yang, H. T.; Wei, W.; Zhang, Y. J.; Liu, S. Q. A Sensitive, Label-Free Electrochemical Detection of Telomerase Activity without Modification or Immobilization. *Biosens. Bioelectron*. **2017**, *91*, 347-353.

41. Tian, Y.; Tatsuma, T. Mechanisms and Applications of Plasmon-Induced Charge Separation at TiO_2 Films Loaded with Gold Nanoparticles. *J. Am. Chem. Soc*. **2005**, *127*, 7632-7637.

42. Gonzalez, R.; Garitaonandia, I.; Crain, A.; Poistovoitov, M.; Abramihina, T.; Noskov, A.; Jiang, C.; Morey, R.; Laurent, L. C.; Elswrth, J. D.; Snyder, E. Y.; Redmond, D. E.; Semechkin, R. Proof of Concept Studies Exploring the Safety and Functional Activity of Human

Parthenogenetic-Derived Neural Stem Cells for the Treatment of Parkinson's Disease. *Cell Transplant*, **2015**, *24*, 681-690.

43. Bian, Z. F.; Tachikawa, T.; Zhang, P.; Fujitsuka, M.; Majima, T. Au/TiO_2 Superstructure-Based Plasmonic Photocatalysts Exhibiting Efficient Charge Separation and Unprecedented Activity. *J. Am. Chem. Soc.* **2014,** *136*, 458−465.

44. Ma, K.; Fox, L.; Shi. G.; Shen, J.; Liu, Q.; Pappas, J. D.; Cheng, J.; Qu, T. Generation of Neural Stem Cell-Like Cells from Bone Marrow-Derived Human Mesenchymal Stem Cells. *Neurol Res.* **2011**, *33*, 1083-1093.

45. Hiyama, E.; Hiyama, K. Telomere and Telomerase in Stem Cells. *Brit. J. Cancer.* **2007**, *96*, 1020-1024.

Table of Contents